Resonant ultrasound spectroscopy of horizontal transversely isotropic samples: Resonant Ultrasound Spectroscopy

Article · June 2015

DOI: 10.1002/2014JB011839

2 authors:

Leighton M. Watson
Stanford University
2 PUBLICATIONS **2** CITATIONS
SEE PROFILE

Kasper Van Wijk
University of Auckland
138 PUBLICATIONS **803** CITATIONS
SEE PROFILE

AGU PUBLICATIONS

JGR

Journal of Geophysical Research: Solid Earth

RESEARCH ARTICLE
10.1002/2014JB011839

Key Points:
- Enables more accurate measurement of the anisotropic properties of rock samples
- Fills frequency gap between seismic and higher-frequency laboratory measurements
- Enables intrinsic attenuation to be estimated

Correspondence to:
L. Watson,
lwat054@stanford.edu

Citation:
Watson, L., and K. van Wijk (2015), Resonant ultrasound spectroscopy of horizontal transversely isotropic samples, *J. Geophys. Res. Solid Earth*, *120*, 4887–4897, doi:10.1002/2014JB011839.

Received 10 DEC 2014
Accepted 4 JUN 2015
Accepted article online 8 JUN 2015
Published online 22 JUL 2015

Resonant ultrasound spectroscopy of horizontal transversely isotropic samples

Leighton Watson[1,2] and Kasper van Wijk[3]

[1]Physical Acoustics Laboratory, Department of Physics, University of Auckland, Auckland, New Zealand, [2]Now at Department of Geophysics, Stanford University, Stanford, California, USA, [3]Physical Acoustics Laboratory and Dodd-Walls Centre for Photonic and Quantum Technologies, Department of Physics, University of Auckland, Auckland, New Zealand

Abstract Most crustal rocks present some amount of directional dependence of seismic speeds, particularly mudstones (also termed "shales"). Hence, accurate imaging of the subsurface requires anisotropic models and integration of rock physics information in order to constrain the inherent nonuniqueness of the inversion from seismic data. Resonant ultrasound spectroscopy provides estimates of the full anisotropic stiffness tensor from resonant frequencies of geological core samples, along with a measure of intrinsic attenuation. We have developed new functionality to existing codes which enable horizontal transversely isotropic samples to be analyzed. We compared and discussed estimations of the elastic properties of mudstone samples with hexagonal symmetry; one sample was drilled parallel and one perpendicular to the layering. While spatial heterogeneity in the mudstone prevented a direct correlation of the elastic parameters of each sample, time-of-flight measurements reveal frequency dispersion of the elastic parameters that is consistent between the samples.

1. Introduction

Most crustal rocks are characterized by an anisotropic seismic wave speed [e.g., *Thomsen*, 1986a]. This directional dependence can be caused by local stress conditions, or the preferential alignment of crystals, grains, fine layers, and microfractures [*Tsvankin*, 2001; *Horne et al.*, 2012]. For example, mudstone formations (i.e., shales) consist of thin-layered sequences of aligned microscopic clay platelets, which are responsible for the inherent anisotropy of mudstones, and can be described by a hexagonal symmetry model [*Horne et al.*, 2012].

Recently, mudstone rocks have become of significant interest to the exploration geophysics community. Technological advances and the development of extraction techniques, such as horizontal well drilling and hydraulic fracturing, have enabled economical recovery of natural gas from mudstone formations [*Horne et al.*, 2012], which comprise about 75% of the clastic fill of sedimentary basins [*Tsvankin*, 2001]. Laboratory measurements of the elastic parameters of crustal material act to calibrate and understand seismic field measurements. Estimating the anisotropic model of the subsurface from seismic data alone is a highly nonunique process [*Bakulin et al.*, 2010]. However, the inherent nonuniqueness of the inversion can be ameliorated if independent estimates of at least one anisotropic model parameter are known [*Grechka et al.*, 2002]. Under favorable circumstances, resonant ultrasound spectroscopy (RUS) can be used to estimate all five anisotropy parameters from a single core sample.

Stress-strain measurements characterize rock samples from static to seismic wavelengths (up to ~100 Hz) [e.g., *Spencer*, 1981; *Adam et al.*, 2006; *Batzle et al.*, 2006]. Time-of-flight measurements in rocks are typically done at ultrasonic frequencies (upward of ~100 kHz) [e.g., *Wang*, 2002; *Blum et al.*, 2013]. In between these, resonant ultrasound spectroscopy inverts the normal modes of an elastic body for its elastic parameters in the kHz range [*Migliori et al.*, 1993], enabling seismic field observations and ultrasonic laboratory measurements to be correlated.

RUS can be used on small, rare, or hard-to-obtain samples [*Migliori and Sarro*, 1997] and enables the complete elastic tensor to be inferred from a single experiment [*Zadler et al.*, 2004]. It is an inverse problem that relies on the underlying principle that the resonant frequencies of a sample depend on the sample's elastic moduli, geometry, and density [*Migliori et al.*, 1993]. The forward problem is to calculate the resonant frequencies from the elastic moduli, sample geometry, and density. The inverse problem is to compute the elastic moduli from

the resonant frequencies, assuming that the geometry and density are known. A misfit function is minimized by the nonlinear Levenberg-Marquardt algorithm [*Levenberg*, 1944; *Marquardt*, 1963]. The forward and inverse calculations are performed using software developed by *Zadler et al.* [2004]. While at a much smaller scale, RUS has many parallels with normal-mode seismology [*Dahlen and Tromp*, 1998].

Isotropic rocks are characterized by two elastic constants. The next lowest order of symmetry of geological interest is anisotropic models with transverse isotropy (also called hexagonal symmetry) [*Thomsen*, 1986a]. These models have a single axis of rotational symmetry with perpendicular isotropic planes and are described by five elastic constants [*Tsvankin*, 2001]. Geological rock samples are often cored parallel or perpendicular to the symmetry axis, termed horizontal or vertical transverse isotropy (HTI and VTI, respectively). For spherical and cubic samples, HTI and VTI symmetries can be described by a single model by applying a rotation of 90° about the symmetry axis. However, most geological samples are cylindrical, and HTI and VTI symmetries in cylindrical samples cannot be described by the same model with a 90° rotation as the dimensions of a cylinder are not the same in all directions.

Zadler et al. [2004] performed resonance measurements on a range of symmetries. We present an extension to their work to include HTI symmetry, enabling a wider range of samples to be measured. We determine the elastic moduli for a VTI and HTI mudstone sample using RUS, investigate joint analysis of the two data sets, and compare the results with time-of-flight measurements.

2. Theoretical Description

We briefly describe the nonzero elements of the stiffness tensor for horizontal and vertical transversely isotropic (HTI and VTI, respectively) media, followed by an explanation of how RUS provides an estimate of this tensor from the resonant modes of the sample.

2.1. Elastic Properties

The properties of an elastic medium are determined by the stiffness tensor (c_{ijkl}) which relates the stress (σ_{ij}) applied to a sample with the strain (ϵ_{kl}) experienced:

$$\sigma_{ij} = c_{ijkl}\epsilon_{kl}. \tag{1}$$

The $3 \times 3 \times 3 \times 3$ elastic tensor c_{ijkl} can be expressed as a 6×6 matrix $c_{\alpha\beta}$ using the Voigt recipe [*Thomsen*, 1986a]:

$$\begin{array}{llcccccccc} ij \text{ or } kl & & 11 & 22 & 33 & 32 = 23 & 31 = 13 & 12 = 21, \\ \downarrow & \downarrow : & \updownarrow & \updownarrow & \updownarrow & \updownarrow & \updownarrow & \updownarrow \\ \alpha & \beta & 1 & 2 & 3 & 4 & 5 & 6 \end{array} \tag{2}$$

so that expression (1) reduces to

$$\sigma_{\alpha} = c_{\alpha\beta}\epsilon_{\beta}. \tag{3}$$

For triclinic symmetry, the most general model of anisotropy, the stiffness tensor has 21 independent components [*Tsvankin*, 2001]. For higher degrees of symmetry the number of independent components is reduced to five parameters for a hexagonal medium and two parameters for a medium that is elastically isotropic. Most crustal rocks display some amount of elastic anisotropy [*Thomsen*, 1986a]. A rock is termed hexagonal or transversely isotropic if it has a single axis of rotational symmetry with perpendicular isotropic planes [*Tsvankin*, 2001] (Figure 1). The stiffness tensor for a hexagonal medium can be expressed with five independent components of the stiffness tensor [*Tsvankin*, 2001]. For a VTI sample the stiffness tensor is

$$c^{v}_{\alpha\beta} = \begin{bmatrix} c^{v}_{12} + 2c^{v}_{66} & c^{v}_{12} & c^{v}_{23} & 0 & 0 & 0 \\ c^{v}_{12} & c^{v}_{12} + 2c^{v}_{66} & c^{v}_{23} & 0 & 0 & 0 \\ c^{v}_{23} & c^{v}_{23} & c^{v}_{33} & 0 & 0 & 0 \\ 0 & 0 & 0 & c^{v}_{44} & 0 & 0 \\ 0 & 0 & 0 & 0 & c^{v}_{44} & 0 \\ 0 & 0 & 0 & 0 & 0 & c^{v}_{66} \end{bmatrix} \tag{4}$$

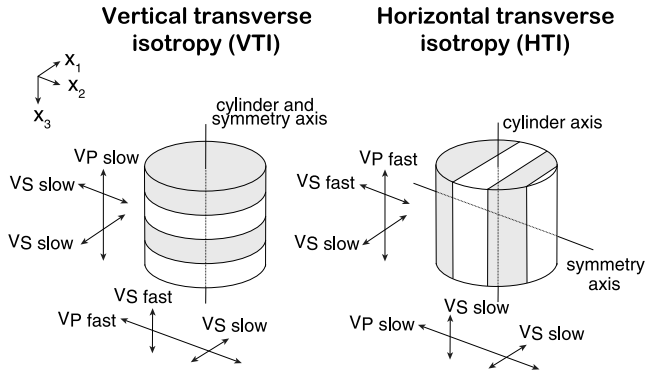

Figure 1. (left) Vertical and (right) horizontal transversely isotropic symmetries with wave speeds annotated. For each symmetry there is a fast and slow direction of propagation for the *P* wave (solid line) and three slow and one fast directions for the polarization of the *S* wave (dashed line). It should be noted that "vertical" and "horizontal" refer to the symmetry axis and not to the orientation of the isotropic planes.

The stiffness tensor for an HTI medium, as defined in Figure 1, is as follows:

$$c^h_{\alpha\beta} = \begin{bmatrix} c^h_{11} & c^h_{12} & c^h_{12} & 0 & 0 & 0 \\ c^h_{12} & c^h_{33} & c^h_{33} - 2c^h_{44} & 0 & 0 & 0 \\ c^h_{12} & c^h_{33} - 2c^h_{44} & c^h_{33} & 0 & 0 & 0 \\ 0 & 0 & 0 & c^h_{44} & 0 & 0 \\ 0 & 0 & 0 & 0 & c^h_{66} & 0 \\ 0 & 0 & 0 & 0 & 0 & c^h_{66} \end{bmatrix} \tag{5}$$

For the coordinate system shown in Figure 1, a 90° coordinate transformation results in the following mapping:

$$\begin{array}{ccccccccc} \text{VTI} & & c^v_{11} & c^v_{12} & c^v_{13} & c^v_{33} & c^v_{44} & c^v_{66} \\ \updownarrow & : & \updownarrow & \updownarrow & \updownarrow & \updownarrow & \updownarrow & \updownarrow \\ \text{HTI} & & c^h_{33} & c^h_{23} & c^h_{12} & c^h_{11} & c^h_{66} & c^h_{44}. \end{array} \tag{6}$$

In a hexagonal medium there is a fast and slow direction of propagation for the *P* wave and direction of polarization for the *S* wave. The relative speed of the *P* and *S* wave polarizations in the different directions of propagation can be determined qualitatively by correlating seismic wave speed to the rigidity of a deck of cards [*Thomsen*, 1986b; *Winterstein*, 1992]. Figure 1 shows the orthogonal seismic wave polarizations in each sample; a fast and a slow *P* wave direction of propagation and one fast and three slow *S* wave polarizations. The wave speeds are related to the elastic moduli for HTI and VTI media by the following:

$$V_{P\,\text{fast}} = \sqrt{\frac{c^v_{11}}{\rho}} = \sqrt{\frac{c^h_{33}}{\rho}}, V_{P\,\text{slow}} = \sqrt{\frac{c^v_{33}}{\rho}} = \sqrt{\frac{c^h_{11}}{\rho}}, \tag{7}$$

$$V_{S\,\text{fast}} = \sqrt{\frac{c^v_{66}}{\rho}} = \sqrt{\frac{c^h_{44}}{\rho}}, V_{S\,\text{slow}} = \sqrt{\frac{c^v_{44}}{\rho}} = \sqrt{\frac{c^h_{66}}{\rho}}. \tag{8}$$

2.2. The Forward Problem

The forward problem is to calculate the expected resonances for a given stiffness tensor and known sample geometry and density. *Zadler et al.* [2004] divided the problem into three sections: (1) variational approximations for resonances, (2) elastic energy and damping, and (3) excitation calculations. The forward problem is solved using the variational Rayleigh-Ritz method. For more information the reader is referred to *Visscher et al.* [1991], *Migliori and Sarro* [1997], and *Zadler et al.* [2004].

2.3. The Inverse Problem

The inverse problem is to estimate the elastic properties given the resonant frequencies of the sample. The elegant Levenberg-Marquardt method is an iterative method that varies smoothly between the steepest descent

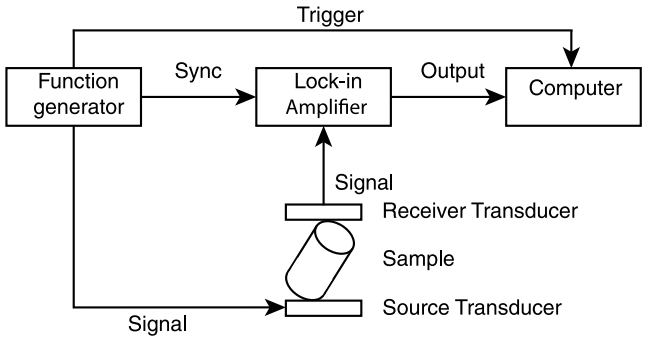

Figure 2. Schematic diagram of resonant ultrasound spectroscopy experimental setup.

method far from the minimum and Newton's method as the minimum is approached [*Press et al.*, 1986]. For an extensive discussion on the Levenberg-Marquardt minimization procedure refer to *Fletcher* [1980], *Press et al.* [1986], or *Migliori and Sarro* [1997].

The Levenberg-Marquardt algorithm [*Levenberg*, 1944; *Marquardt*, 1963] is used to adjust the model parameters (the components of $c_{\alpha\beta}$) in order to minimize the misfit between the measured ($f^{(m)}$) and predicted ($f^{(p)}$) resonant frequencies, defined as

$$\chi^2 = \frac{1}{N}\sum_i^N w_i \left(\frac{f_i^{(m)} - f^{(p)}}{\sigma_i^{(m)}} \right)^2, \tag{9}$$

where N is the number of measured modes, $\sigma^{(m)}$ is the estimated uncertainty in each mode, and w is the weight given to each mode. For observed modes $w = 1$. For modes predicted by the forward model but either unobserved or unclear in the measurements $w = 0$. Some resonant modes may go undetected in the measurements, either because they are not excited in the acquisition geometry or because modes are overlapping. Zero weights of these expected—but not observed—resonances do not contribute to χ^2 but enable the observed resonances to be paired with the correct modeled resonant modes. Intermediate values of w can be used based on the confidence of each peak. A value of $\chi^2 = 1$ indicates that the model predicts the measured data up to one standard deviation, on average; often this value is chosen as the "target."

Figure 3. Photographs of the (left) vertical and (right) horizontal transversely isotropic mudstone cores showing the layering in the curved side of the vertical transversely isotropic sample and in the flat face of the horizontal transversely isotropic sample. There is a marked difference in color between the two samples despite being cored centimeters apart. It is worth noting that the visual fabric does not always correspond with elastic anisotropy [*Adam et al.*, 2014].

3. Experimental Design

A function generator (Stanford Research Systems, DS345) sends a sinusoidal signal (10 V peak to peak) to a contacting piezoelectric source transducer (Olympus NDT V101/V151), sweeping across a range of frequencies. Resulting displacements propagate through the rock sample and are detected by another contacting transducer. The sample is positioned on edge between the two transducers, as shown in Figure 2, in order to excite the maximum number of modes [*Zadler et al.*, 2004]. An aluminum counterweight in the sample holder minimizes the loading of the top transducer and hence the perturbation of the observed resonances by external weighting [*Zadler*, 2005]. The measured signal is passed to a Digital Signal Processing lock-in amplifier (Stanford Research Systems, SR850) and divided into a component x, in phase, and a component y,

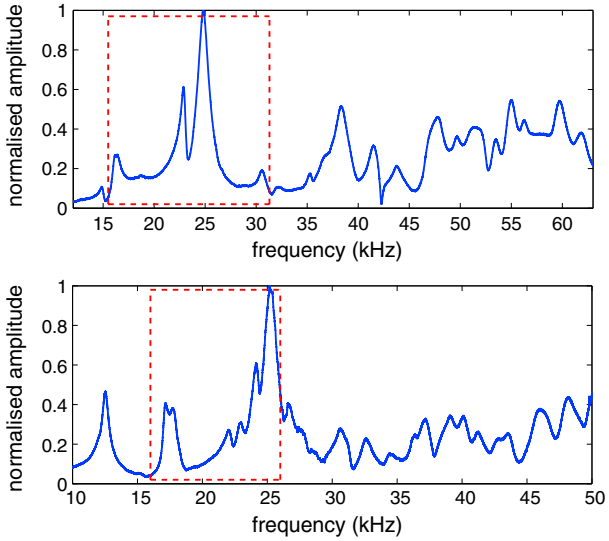

Figure 4. Spectra for the (top) vertical and (bottom) horizontal transversely isotropic samples. The dashed box indicates the area focused on in Figure 5. The spectra becomes more complicated at higher frequencies.

out of phase, with the lock-in reference signal. The magnitude of the two components $R = \sqrt{x^2 + y^2}$ is recorded with 14 bits dynamic range with a PCI digital oscilloscope card (Alazar Tech ATS9440) housed in a desktop computer.

We measured the resonant spectra of a horizontal and a vertical transversely isotropic (HTI and VTI, respectively) core sample of a mudstone rock collected from an outcrop in Montana [*Blum et al.*, 2013]. The VTI sample is the same sample investigated by *Blum et al.* [2013] and that they referred to as MSH, while the HTI sample was cored specifically for this study. Despite the two cylindrical cores being drilled within centimeters of each other, the samples display considerable variation; they look different (Figure 3), and the density of the VTI sample is 2.1 g/cm^3 compared to 1.7 g/cm^3 for the HTI sample. The VTI sample is 5.88 cm high with a diameter of 3.80 cm, and the HTI sample is 5.39 cm high with a diameter of 3.76 cm.

The forward and inverse calculations are performed using software developed by *Zadler et al.* [2004]. The forward code is able to model a range of symmetries from isotropic to orthorhombic. However, for hexagonal symmetry there are two subcases that are regularly encountered in geophysical measurements, VTI and HTI. Previously, only VTI hexagonal samples were considered. Here we present an extension of the previous work to HTI media.

4. Results

Resonant spectra for the horizontal and vertical transversely isotropic (HTI and VTI, respectively) samples are shown in Figure 4. The part of the spectrum in the dashed boxes are further discussed in Figure 5. The mean and standard deviation of the resonant frequencies are estimated from repeated measurements. We identify 25 resonant modes of the HTI sample below 50 kHz (Table 1) and 26 for the VTI sample below 72 kHz (Table 2). The different frequency limits are because we had to measure the VTI sample up to higher frequencies than the HTI sample in order to observe a sufficient number of peaks to constrain the inversion [*Migliori and Sarro*, 1997].

The peaks are identified visually and, starting from the low-frequency modes that we can confidently identify, are matched to the peaks predicted by the forward model. If we miss a mode or if the modes are matched incorrectly, the

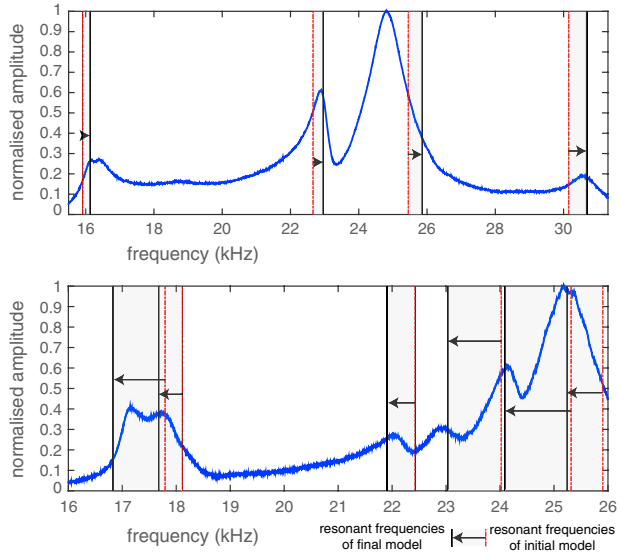

Figure 5. Section of the resonant spectra (as indicated in Figure 4) for (top) vertical and (bottom) horizontal transversely isotropic samples. The resonant frequencies of the initial (red, dashed) and final (black, solid) models are shown, indicating how the inversion procedure iterates from the initial to final model improving the fit to the majority of observed resonant frequencies.

Table 1. Comparison of Measured ($f^{(m)}$) and Predicted ($f^{(p)}$) Resonant Frequencies of the Horizontal Transversely Isotropic Mudstone[a]

$f^{(m)}$ (Hz)	$f^{(p)}$ (Hz)	$\sigma^{(m)}$ (Hz)	$\left(\frac{f^{(p)}-f^{(m)}}{\sigma^{(m)}}\right)^2$	freq. #
12,473	11,814	55	143.56	1
14,740	15,000	70	13.80	2
17,150	16,821	61	29.09	3
17,782	17,665	74	2.50	4
22,108	21,910	46	18.53	6
22,940	23,033	88	1.12	7
24,182	24,060	105	1.35	10
25,247	25,244	87	0.00	11
27,473	27,888	267	2.42	12
28,620	28,184	82	28.27	14
30,307	30,028	266	1.10	16
31,360	31,151	246	0.72	20
32,743	33,008	170	2.43	21
34,580	34,670	56	2.58	22
36,100	36,094	71	0.01	26
37,364	37,549	148	1.56	29
39,126	38,814	333	0.88	31
39,860	39,725	368	0.13	34
41,072	40,801	260	1.09	38
42,463	42,624	251	0.41	40
43,535	43,677	117	1.47	43
45,998	45,887	451	0.06	47
47,120	47,529	57	51.49	50
48,314	48,603	201	2.07	52
49,617	49,600	298	0.00	57

[a] $\sigma^{(m)}$is the uncertainty in each frequency calculated from repeated measurements, and the fourth column lists the relative contribution of individual modes to the total χ^2; freq # is the number of the identified mode.

inversion diverges. Hence, we are manually checking the pairing between observed and predicted resonant modes as we add more modes to the inversion. For more details on the methodology the reader is referred to *Zadler et al.* [2004] and Appendix D from *Zadler* [2005].

4.1. Elastic Constants

The inversion minimizes the sum of the difference between the measured and predicted modes. The fit for an isotropic model to the data for both samples led to χ^2 value of 87 and 154 for the VTI and HTI samples, respectively. Using hexagonal models resulted in a substantially improved fit with χ^2 decreasing to 8.6 and 6.5, respectively.

The first mode is excluded (given a weight of $w = 0$) because of the reported "curious property" of RUS measurements that the first one or two modes never fit well, regardless of apparatus, sample type or transducers [*Migliori and Sarro*, 1997]. This is illustrated by the large misfit of the first mode for both samples, as shown in Tables 1 and 2. Beyond the first mode, individual predicted modes in the final model may be a less accurate fit to the data than the initial model, but overall, the final model is a better fit to the measurements. This is shown in Figure 5 (top) where the final model fits the measured peak at 25 kHz worse than the initial model. However, the inversion procedure improves the fit for the other three resonant modes, and the overall fit for all observed modes. The anisotropic elastic parameter estimates, and the resulting seismic wave speeds are shown in Table 3.

Table 2. Comparison of Measured ($f^{(m)}$) and Predicted ($f^{(p)}$) Resonant Frequencies of the Vertical Transversely Isotropic Mudstone[a]

$f^{(m)}$ (Hz)	$f^{(p)}$ (Hz)	$\sigma^{(m)}$ (Hz)	$\left(\frac{f^{(p)}-f^{(m)}}{\sigma^{(m)}}\right)^2$	freq. #
14,897	15,335	22	396.37	1
16,334	16,131	136	2.23	2
22,977	22,961	82	0.04	3
24,810	25,860	259	16.44	4
30,587	30,671	13	41.75	5
35,310	35,060	118	4.49	8
36,550	37,542	234	17.97	9
38,589	39,018	104	17.02	11
41,706	41,813	199	0.29	12
42,513	42,638	225	0.31	13
43,800	43,703	142	0.47	15
46,720	46,006	85	70.56	17
48,027	48,408	212	3.23	18
49,488	49,581	59	2.48	21
51,342	50,758	144	16.45	22
52,343	52,339	240	0.00	23
53,490	53,702	160	1.76	24
54,537	54,803	253	1.11	27
56,273	55,941	112	8.79	28
59,854	60,285	380	1.29	30
61,740	61,005	471	2.44	34
64,193	64,164	194	0.02	37
66,320	65,875	246	3.27	40
67,193	66,743	247	3.32	41
68,042	68,046	112	0.00	42
69,950	70,062	154	0.53	44

[a] $\sigma^{(m)}$ is the uncertainty in each frequency calculated from repeated measurements and the fourth column lists the relative contribution of an individual mode to the total χ^2; freq # is the number of the identified mode.

4.2. Attenuation

Attenuation is a process that dissipates the energy of elastic waves and alters their amplitude and frequency content [*Aki and Richards*, 1980]. RUS can provide important information about the intrinsic attenuation (absorption) of seismic energy, as a function of frequency. Attenuation information can be used to supplement velocity information when inferring pore fluid conditions and physical properties of a sample [*Toksöz et al.*, 1979; *Adam and van Wijk*, 2014]. Attenuation is inversely related to the quality factor

$$Q = \frac{\omega_0}{\delta\omega}, \tag{10}$$

where ω_0 is the resonant frequency and $\delta\omega$ is the full width at half maximum displacement.

We determine the Q factor by fitting a Breit-Wigner model to the observed data using *fitspectra* [*Zadler*, 2005]. Figure 6 shows the estimate of Q as a function of frequency. The mean Q value is 40.1 and 37.6 for the VTI and HTI samples, respectively. A linear fit to the mean Q values indicates that the Q factor may increase with frequency, although the error bars on the attenuation estimates are large enough to support a constant Q model.

4.3. Time-of-Flight Measurements

We measured the time of flight of seismic waves through the samples using the same contacting transducers as in the RUS measurements, excited with a waveform with a dominant frequency of 500 kHz generated by

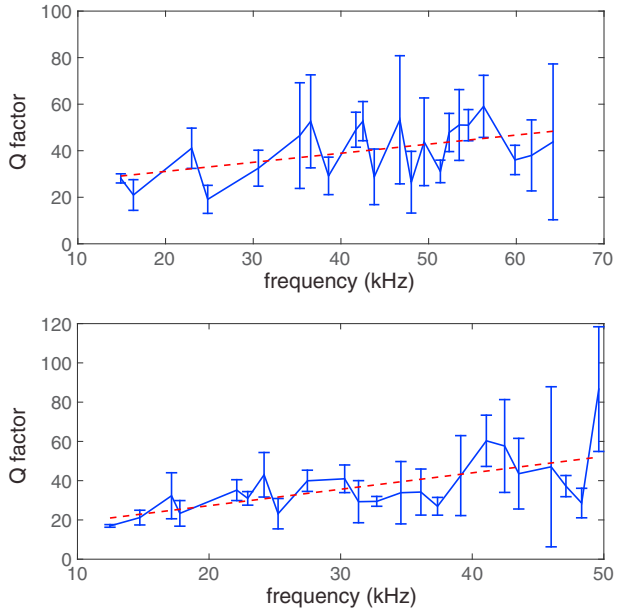

Figure 6. *Q* values as a function of frequency for the (top) vertical and (bottom) horizontal transversely isotropic samples. The dashed line is the best linear fit through the mean *Q* values.

an Olympus NDT pulser. The estimated elastic moduli are shown in Table 3. Figure 7 compares the seismic wave speeds between resonance and time-of-flight measurements. Note that the mean of the wave speed increases with frequency for seven of the eight estimated seismic phase velocities.

5. Discussion

Next, we discuss the implications of RUS measurements on horizontal transversely isotropic (HTI) samples, along with the attenuation and dispersion estimates.

5.1. Why Measure Horizontal Transverse Isotropy Symmetries?

It is useful to be able to perform RUS measurements on HTI samples for a range of reasons. First, the only sample available may have HTI symmetry. Machining it into a VTI sample may not be possible if the sample is too small or too rare to damage.

Table 3. Summary of Elastic Constants (GPa) and Seismic Velocities (m s^{-1}) for Horizontal and Vertical Transversely Isotropic Mudstone[a]

Horizontal Transversely Isotropic (HTI) Mudstone				
RUS				
c_{11}	c_{33}	c_{12}	c_{44}	c_{66}
11.4 ± 1.0	14.5 ± 1.0	4.9 ± 0.3	4.3 ± 0.2	2.1 ± 0.1
$V_{P\,\mathrm{fast}}$	$V_{P\,\mathrm{slow}}$	$V_{S\,\mathrm{fast}}$	$V_{S\,\mathrm{slow}}$	
2920 ± 100	2590 ± 100	1590 ± 40	1110 ± 30	
Time of Flight				
c_{11}	c_{33}	c_{12}	c_{44}	c_{66}
12.3 ± 0.9	16.1 ± 0.9	NA	4.8 ± 0.3	3.4 ± 0.3
$V_{P\,\mathrm{fast}}$	$V_{P\,\mathrm{slow}}$	$V_{S\,\mathrm{fast}}$	$V_{S\,\mathrm{slow}}$	
3080 ± 90	2690 ± 100	1680 ± 50	1410 ± 60	
Vertical Transversely Isotropic (VTI) Mudstone				
RUS				
c_{33}	c_{23}	c_{12}	c_{44}	c_{66}
17.4 ± 0.8	4.9 ± 0.6	7.3 ± 0.4	6.8 ± 0.2	6.6 ± 0.2
$V_{P\,\mathrm{fast}}$	$V_{P\,\mathrm{slow}}$	$V_{S\,\mathrm{fast}}$	$V_{S\,\mathrm{slow}}$	
3120 ± 50	2880 ± 70	1770 ± 30	1800 ± 30	
Time of Flight				
c_{33}	c_{23}	c_{12}	c_{44}	c_{66}
20.1 ± 1.4	NA	6.4 ± 2.4	6.6 ± 0.6	9.3 ± 0.9
$V_{P\,\mathrm{fast}}$	$V_{P\,\mathrm{slow}}$	$V_{S\,\mathrm{fast}}$	$V_{S\,\mathrm{slow}}$	
3450 ± 110	3090 ± 110	2100 ± 100	1770 ± 80	

[a]Model uncertainty in the c_{ij} estimates is estimated from the data uncertainty in the resonant frequencies and propagated through the inversion procedure to the elastic constants and seismic velocities. NA: not available.

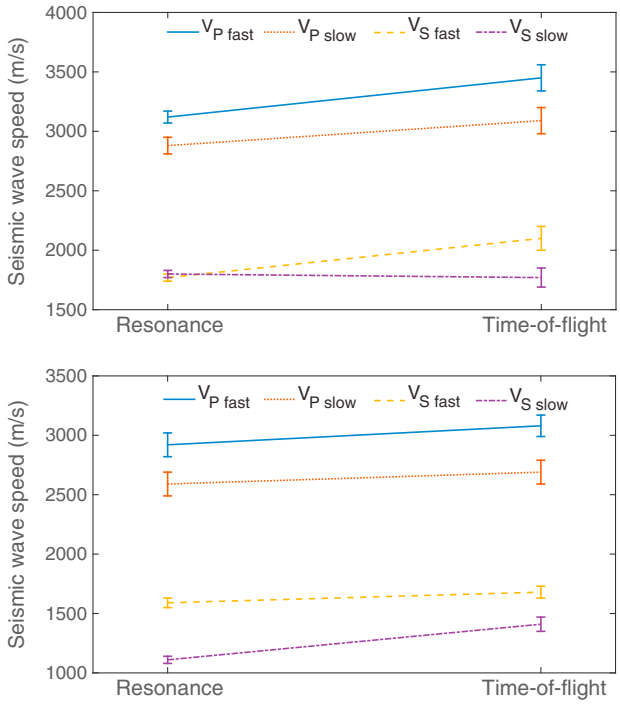

Figure 7. Seismic wave speed as a function of frequency for the (top) vertical and (bottom) horizontal transversely isotropic mudstones. Seismic wave speeds increase with frequency. The mean seismic velocity is greater for the time-of-flight (~10^{5-6} Hz) measurements than the RUS (~10^4 Hz) results for seven out of the eight measured velocities.

Second, mutually perpendicular samples (HTI and VTI) from the same rock provide complementary information. The different samples have modes that are most sensitive to different elastic constants. For example, $V_{P\,\mathrm{slow}}$ and $V_{S\,\mathrm{slow}}$ can be more easily calculated from the measurements on the VTI sample and then used to constrain the inversion of the HTI sample for estimates of the remaining unknowns. Conversely, $V_{P\mathrm{fast}}$ and $V_{S\mathrm{fast}}$ can be determined from the HTI sample and used as starting values in the inversion for the VTI sample. This method of using information from a sample to constrain the inversion of the other promises to be more successful than inverting the resonant frequencies for each symmetry individually. Unfortunately, the correlation between the properties of the samples is low in our case. The color and density of the two cores were substantially different, and we conclude that the elastic moduli, the seismic wave speeds, and the quality factor differ as well.

Third, time-of-flight measurements as a function of angle, such as those discussed by *Wang* [2002] and *Blum et al.* [2013] require HTI symmetry. To understand the dispersive properties of such rocks, RUS measurements on the same sample are desirable.

Fourth, we observe that flexural modes are present in VTI samples, but not for HTI samples. Flexural modes are resonances in which the energy travels along paths that are tilted with respect to the symmetry axis and occur in pairs with the same frequency called doublets or degenerate modes [*Zadler et al.*, 2004]. For a given frequency range there are the approximately the same number of modes for both symmetries. As the VTI sample contains many doublets (for the mudstone sample measured approximately 70% of predicted modes were flexural modes) and only single modes are observed for HTI samples, we will have more distinctly observable resonances for HTI samples. This provides more information which can be used in the inversion. Between 12 and 50 kHz 26 distinct modes were observed for the HTI sample compared to only 14 for the VTI sample. As the complexity of the spectra increases with frequency, this means that it can be easier to perform RUS measurements on HTI than on VTI samples.

One important complication should be mentioned for RUS experiments in HTI cylinders. We performed six sweeps for each sample: three sweeps use V101 and three use V151 transducers. The V101 and V151 transducers are designed to excite *P* and *S* waves, respectively, and hence, using both sets of transducers enables more resonant modes to be observed. To estimate the uncertainty in each resonance, the sample is remounted, rotated about the cylinder axis, and remeasured 6 times. Here the samples are rotated by 120° between realizations. For a perfectly VTI sample, rotation about the cylinder axis has no effect on the measured spectra, as the sample remains pinned between the same layers and the same modes will be excited. For an HTI sample, however, rotating the sample causes the transducers to be pinned between different isotropic planes. This leads to significant changes in the observed spectra as seen in Figure 8 (bottom): when the sample is rotated, a previously indistinct peak at 15 kHz is excited and clearly observable. Therefore, HTI samples require the measurement of resonant spectra with source and receivers at different angles, in order to identify all the resonant modes. Real rocks, however, can have considerable heterogeneities. Therefore, it is good practice to rotate both VTI and HTI samples and collect data from many pinning positions.

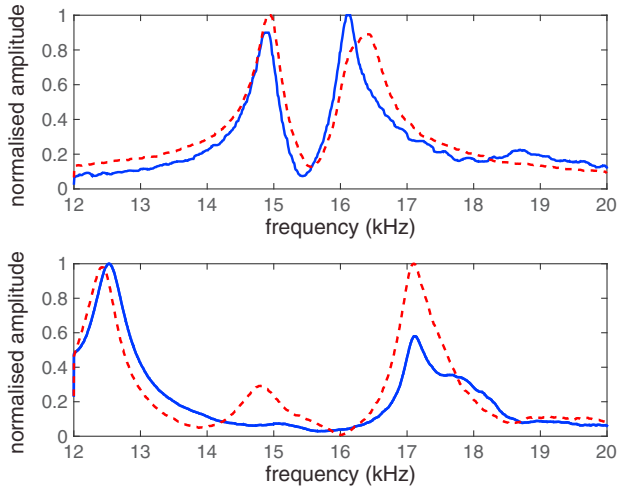

Figure 8. Spectra for the (top) vertical and (bottom) horizontal transversely isotropic mudstones with the samples rotated and remounted between the two measurements shown. When the vertical transversely isotropic mudstone is rotated, the transducers remain on the same isotropic plane and the spectra is similar between measurements. For the horizontal transversely isotropic sample, rotation causes the transducers to move between isotropic planes exciting different resonances, such as the peak at 15 kHz visible in one sweep (red, dashed) but not in the other (blue, solid).

5.2. Best Fits of the Data and Heterogeneity

Inversions of our samples under the assumption of isotropy led to χ^2 values of 87 and 154 for the VTI and HTI samples, respectively. The χ^2 values after inversion assuming hexagonal symmetry are 8.6 and 6.5 for the VTI and HTI samples, respectively. The isotropic model is a better—or less bad—fit to the VTI sample than the HTI sample. This is because both an isotropic and a VTI cylinder are axisymmetric and share some of the same modes, whereas the HTI sample is not symmetric about the cylinder axis and has different resonances.

For hexagonal models, however, not all modes were observed in every sweep, and hence, for some peaks the standard deviation $\sigma^{(m)}$ was calculated using less than six data points. This may have resulted in an underestimation of the uncertainty in the mode and hence an overestimation of χ^2. We estimate an average $\sigma^{(m)}$ calculated from those peaks which are observed in more than 50% of all sweeps. In this case χ^2 decreases to 3.9 and 1.6 for the VTI and HTI samples, respectively. Nevertheless, it is likely that small-scale heterogeneity in the samples—subparallel bedding structures or inclusions within the mudstone—prevent a hexagonal model to predict the observed resonances to within 1 standard deviation.

5.3. Attenuation and Dispersion

One of the advantages of the Q estimates with RUS is that it isolates intrinsic Q [*Zadler*, 2005]. Time domain measurements often estimate attenuation by comparing the amplitude of the first arrival with that of the input signal, neglecting scattered energy that arrives later in the coda. Therefore, the attenuation measured is a combination of intrinsic attenuation, due to the conversion of elastic energy into heat and scattering. In the time domain it can be challenging to differentiate between these two phenomena [*van Wijk et al.*, 2004]. In RUS we measure in the frequency domain over a period of time. Therefore, all scattered energy arrives at the receiver and is included in the calculations of Q, thereby isolating intrinsic Q from the attenuation due to scattering. It is not the measuring in the frequency domain that is important, but rather the fact that RUS measurements are performed over a period of time allowing the scattered energy to reach the receiver.

Our damping estimates on dry rocks at atmospheric pressure are not representative of what would be observed under reservoir conditions but are nonetheless indicative of the capabilities of RUS. When core samples are removed from depth, the reduction in overlying pressure can create microfractures within the sample causing induced anisotropy, decreasing the Q factor, and resulting in greater attenuation. In addition, drying of our samples may have increased the amount of anisotropy [*Blum et al.*, 2013]. Nevertheless, we observe Q to be constant or increasing with frequency, as we do for the seismic wave speeds. This is in concordance with viscoelastic models, in general, and the work on mudstones by *Batzle et al.* [2014], in particular.

6. Conclusion

The characterization of anisotropic media in terms of its elastic properties is likely to benefit from new capabilities in resonant ultrasound spectroscopy that combine broadband measurements in samples with different axes of symmetry. We applied this approach to mudstones cored horizontally and vertically. The samples discussed here displayed considerable inhomogeneity, limiting the conclusions that can be drawn. For compositionally equivalent samples with different symmetries, jointly analyzing the data may lead to improved results.

The extension of RUS to HTI symmetries enables a wider range of samples to be analyzed and allows for better comparison with time-of-flight measurements, providing additional insights about dispersion of the elastic properties. Furthermore, resonance methods are shown to be useful for estimating intrinsic attenuation.

Acknowledgments
Experimental data and updated forward and inverse modeling codes are available at https://github.com/PALab/RUS. This work builds upon previous efforts of Brian Zadler, Jérôme Le Rousseau, John Scales, and Martin Smith. We thank Ludmila Adam for her discussions about anisotropy, attenuation, and dispersion, as well as for her help in sample preparation. We appreciate the constructive comments of the reviewers that improved this manuscript.

References

Adam, L., and K. van Wijk (2014), Introduction to this special section: Attenuation dispersion, *The Leading Edge*, *33*(6), 604–605, doi:10.1190/tle33060604.1.

Adam, L., M. Batzle, and I. Brevik (2006), Gassmann's fluid substitution and shear modulus variability in carbonates at laboratory seismic and ultrasonic frequencies, *Geophysics*, *71*(6), F173–F183, doi:10.1190/1.2358494.

Adam, L., F. Ou, L. Strachan, J. Johnson, K. van Wijk, and B. Field (2014), Mudstone *P*-wave anisotropy measurements with non-contacting lasers under confining pressure, in *SEG Technical Program Expanded Abstracts*, pp. 2749–2754, Society of Exploration Geophysicists, Denver, Colo., doi:10.1190/segam2014-0999.1

Aki, K., and P. G. Richards (1980), *Quantitative Seismology: Theory and Practice*, Freeman, San Francisco.

Bakulin, A., M. Woodward, D. Nichols, K. Osypov, and O. Zdraveva (2010), Localized anisotropic tomography with well information in VTI media, *Geophysics*, *75*(5), D37–D45, doi:10.1190/1.3481702.

Batzle, M. L., D.-H. Han, and R. Hofmann (2006), Fluid mobility and frequency-dependent seismic velocity—Direct measurements, *Geophysics*, *71*(1), N1–N9, doi:10.1190/1.2159053.

Batzle, M. L., G. Kumar, R. Hoffman, L. Duranti, and L. Adam (2014), Seismic-frequency loss mechanisms: Direct observations, *The Leading Edge*, *33*, 656–662, doi:10.1190/tle33060656.1.

Blum, T. E., L. Adam, and K. van Wijk (2013), Noncontacting benchtop measurements of the elastic properties of shales, *Geophysics*, *78*, 25–31, doi:10.1190/geo2012-0314.1.

Dahlen, F., and J. Tromp (1998), *Theoretical Global Seismology*, Princeton Univ. Press, Princeton, N. J.

Fletcher, R. (1980), *Practical Methods of Optimization*, vol. 1, John Wiley, New York.

Grechka, V., I. Tsvankin, A. Bakulin, J. O. Hansen, and C. Signer (2002), Joint inversion of PP and PS reflection data for VTI media: A North Sea case study, *Geophysics*, *67*(5), P1382–P1395, doi:10.1190/1.1512784.

Horne, S., J. Walsh, and D. Miller (2012), Elastic anisotropy in the Haynesville Shale from dipole sonic data, *First Break*, *30*, 37–41, doi:10.3997/1365-2397.2011039.

Levenberg, K. (1944), A method for the solution of certain non-linear problems in least squares, *Q. Appl. Math.*, *2*, 164–168.

Marquardt, D. W. (1963), An algorithm for least-squares estimation of nonlinear parameters, *J. Soc. Ind. Appl. Math.*, *11*, 431–441, doi:10.1137/0111030.

Migliori, A., and J. L. Sarro (1997), *Resonant Ultrasound Spectroscopy*, John Wiley, New York.

Migliori, A., J. L. Sarro, W. M. Visscher, T. M. Bell, M. Lei, Z. Fisk, and R. G. Leisure (1993), Resonant ultrasound spectroscopic techniques for measurement of the elastic moduli of solids, *Physica*, *183*, 1–24, doi:10.1016/0921-4526(93)90048-B.

Press, W. H., B. P. Flannery, S. A. Teukolsky, and W. T. Vetterling (1986), *Numerical Recipes*, Cambridge Univ. Press, Cambridge.

Spencer, J. W. (1981), Stress relaxations at low frequencies in fluid-saturated rocks: Attenuation and modulus dispersion, *J. Geophys. Res.*, *86*(B3), 1803–1812, doi:10.1029/JB086iB03p01803.

Thomsen, L. (1986a), Weak elastic anisotropy, *Geophysics*, *51*, 1954–1966, doi:10.1190/1.1442051.

Thomsen, L. (1986b), Reflection seismology in azimuthally anisotropic media, *SEG Expanded Abstracts*.

Toksöz, M. N., D. H. Johnston, and A. Timur (1979), Attenuation of seismic waves in dry and saturated rocks: I. Laboratory measurements, *Geophysics*, *44*, 681–690, doi:10.1190/1.1440969.

Tsvankin, I. (2001), *Seismic Signatures and Analysis of Reflection Data in Anisotropic Media*, Elsevier Science, Cambridge.

van Wijk, K., M. Haney, and J. A. Scales (2004), 1D energy transport in a strongly scattering laboratory model, *Phys. Rev. E: Stat. Nonlinear Soft Matter Phys.*, *69*, 036611, doi:10.1103/PhysRevE.69.036611.

Visscher, W. M., A. Migliori, T. M. Bell, and R. A. Reinert (1991), On the normal modes of free vibration of inhomogeneous and anisotropic elastic objects, *Acoust. Soc. Am.*, *90*, 2154–2162, doi:10.1121/1.401643.

Wang, Z. (2002), Seismic anisotropy in sedimentary rocks: Part 2. Laboratory data, *Geophysics*, *67*(5), 1423–1440, doi:10.1190/1.1512743.

Winterstein, D. (1992), How shear-wave properties relate to rock fractures, *The Leading Edge*, *30*, 21–28, doi:10.1190/1.1436900.

Zadler, B. (2005), Properties of elastic materials using contacting and non-contacting acoustic spectroscopy, PhD thesis, Colorado School of Mines, Golden.

Zadler, B. J., J. H. L. Le Rousseau, J. A. Scales, and M. L. Smith (2004), Resonant ultrasound spectroscopy: Theory and application, *Geophys. J. Int.*, *156*, 154–169, doi:10.1111/j.1365-246X.2004.02093.x.